

TEMPERATURE COMPENSATED TRANSFER FUNCTION FOR PROBABILITY OF DETECTION (POD) IN HIGH TEMPERATURE ULTRASONIC NDE USING LOW TEMPERATURE SIGNALS

Prathamesh N. Bilgunde and Leonard J. Bond

Department of Aerospace Engineering
Iowa State University, Ames, IA 50011
pratham@iastate.edu, bondlj@iastate.edu

ABSTRACT

Ultrasonic piezoelectric based transducers offer the potential for in-coolant NDT measurements and imaging required at high temperature for the safe operation of advanced small modular reactors (SMRs). Current work estimates a significant 97% reduction in the probability of detection (POD) for an artificial flaw size of 2λ due to degradation of the transducer performance at elevated temperature. The source of variability for POD in the current work is the temperature dependence of material matrix of piezoelectric material PZT-5A used in the sensor. The physics based model developed using finite element method quantifies reduction in the scattering amplitude for the side drilled hole (SDH) from 15 C to 195C. Using model assisted probability of detection (MAPOD) approach, sensor temperature effect on the POD is demonstrated for SDHs in the low carbon steel specimen. Scattering amplitudes for the room temperature simulated data is validated with the experimental data. A temperature correction factor and transfer factors are reported to transform the simulated temperature effect from physics based model to the experimental data for estimation of high temperature POD using low temperature ultrasonic measurements.

Keywords: MAPOD, piezoelectric, finite element, high temperature, nuclear reactor

1 INTRODUCTION

Generation IV fast nuclear reactors are being developed to support sustainable development, economic competitiveness, and improved safety [1]. Past experience, specifically, with regard to long term maintenance experience from the Phoenix reactors (France) has underlined the need to provide effective and reliable inspection of components [2]. The efficacy of the NDT inspection is often quantified by the probability of detection (POD) curve. Previous studies have shown that signal to noise ratio (S:N) becomes a critical issue for transducers operating in liquid sodium at a hot stand-by temperature of 260 C[3]. Particularly, the reduction in the signal strength as a function of temperature reduces the ability to identify and distinguish between an ultrasonic response from the defect and electrical noise. This reduction in signal strength can cause a reduction in POD in a high temperature (HT) environment that needs to be predicted.

From POD perspective, actual non-destructive inspection is highly variable due to human factors, experimental limitations etc. However, these experiments are time consuming and expensive due to the cost of the defects that need to be fabricated into the samples. A more cost-effective approach to increase confidence is using physics based modeling to predict POD, and this has been demonstrated for many years [4]. Sarkar et al. [5] proposed a modeling methodology to estimate POD as a function of known fixed effect parameters. These models have been an integral part of a unified approach for model assisted probability of detection (MAPOD)[6][7]. The basic idea behind MAPOD is to use an understanding of the effects of physical factors on the measurement results [6]. Cobb et al. [8] advocated development of hybrid finite element models to use in the MAPOD approach. The thesis of this work states that predictive modeling should be multi-domain consisting of sensor, electronics, and power management. Crack geometry was the primary source of variability in this work [8]. Smith et al. developed the Full Model-Assisted (FMAPOD) approach which was validated with results using the MIL-HDBK-1823 approach [9]. Smith [10] also presented a transfer function approach that correlated the responses from an artificial defect to that of a real crack geometry. In 2011, Aldrin et al. [11] reported simulation-based POD studies for reliability assessment

of structural health monitoring (SHM) systems within the framework of MAPOD. Jensen et al. [12] explored uncertainty propagation through CIVA simulation models. Wirdelius et al. [13] also developed POD based on synthetic data obtained from simSUNDT software. Pavlovi et al. [14] reported POD data as a function of multiple parameters in contrast to the conventional signal response analysis. Li et al. [15] developed a statistical model for estimating POD based on the physical mechanisms of ultrasonic inspection. This work [15] successfully demonstrates the intersection of statistical and physical modeling of ultrasonic wave propagation for the purpose of estimating POD.

In a harsh operating environment, such as a nuclear reactor, POD is expected to reduce over time due to deterioration of sensor performance. In 2014, Subair et al. [16] reported finite element modeling for the estimation of POD of nuclear components at room temperature. Roy et al. [17] developed temperature dependent, physics based modeling using experimental data up to 80 C. The objective of this work [17] was to propose a temperature compensation strategy for guided waves. Similarly, Wang et al. [18] reported an adaptive filtering technique for temperature compensation of Lamb waves. Recently, Salmanpour et al. [19] proposed a new method of temperature correction and used it in conjunction with a delay and sum damage detection algorithm. The proposed method is based on baseline signal stretch with an improved minimum residual allowing correction over a larger temperature range. Gianneo et al. [20] reported the FMAPOD approach for inspection of a copper canister to plot the POD curve for flat bottom holes (FBH) where data were calculated using CIVA. In this work, the primary source of variability was structural attenuation. Gianneo [21] extended this work using finite element models for a multi-parameter POD formulation for a Lamb waves-based SHM for light alloy aeronautical plates. Yusa et al. [22] evaluated general effects of flaw signals using the numerical simulations and scattering of signals using experimental measurements. Recently, Janapati et al. [23] discussed role of POD in NDE and SHM. The focus of this work was quantifying the effect of transducer parameters on damage detection sensitivity.

However, the effect of temperature dependency of piezoelectric material on the POD is not sufficiently quantified. In the current work, temperature dependency of PZT-5A is modelled with regards to its effect on the POD. The objective of this work is to connect a microscopic material phenomenon that occurs within piezoelectric ceramics at a high temperature to an industrial practice of evaluating POD for quantifying performance of NDT inspections. This is achieved by a physics based model using finite element (FE) software COMSOL and temperature dependent material coefficients of PZT-5A [24]. Using the FE model, temperature correction and transfer factors are proposed to estimate POD value at high temperature using POD of room temperature experimental data.

2 PROBLEM DESCRIPTION

The problem considered in this work consists of a planar compression wave transducer transmitting at normal incidence through a solid-solid interface as shown in Fig.1. The elastic waves are scattered by the side drilled hole (SDH) in the solid and the response is received by the same transducer in a pulse-echo contact experiment. It is assumed that the plane of transducer is perpendicular to the axis of the SDH.

The assumptions for the physics based model are: a) plain strain condition, b) the material behaves linearly elastic, c) small deformation of the plate, d) material is continuous and homogenous, d) damping variation due to temperature is negligible, d) the thermoelectric coupling resulting in a pyroelectric effect is not considered, and e) electric field of piezoelectric material is irrotational (quasi-electrostatic field which implies absence of magnetization). Thus, the frequency dependence of the piezoelectric material is caused only by the mechanical displacement.

Let Ω be the domain of the problem connected by the Lipschitz boundaries $\partial\Omega$. The low carbon steel block of 30.0 mm x 30.0mm cross section and the piezoelectric transducer are represented by domain Ω_{steel} and $\Omega_{\text{transducer}}$ respectively. The piezoelectric material PZT-5A domain has a length of 6.0 mm and a thickness of 1.0mm. Hence, the computational domain is given by $\Omega = \Omega_{\text{steel}} \cup \Omega_{\text{transducer}}$. In this approach, the

amplitude of the signal reflected from SDHs is computed in terms of the vertical component of the displacement field in the finite element model.

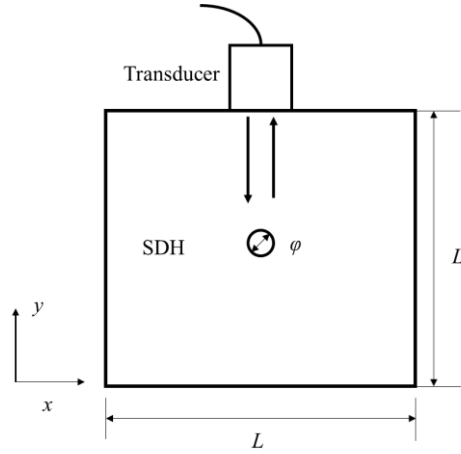


Figure 1. Problem configuration to predict the response from SDHs at normal incidence

3 PHYSICS BASED MODEL

3.1 Constitutive equations of piezoelectric material for temperature dependence

The total internal energy density of the piezoelectric material is given by the mechanical and electrical work done which is given as

$$dU = \sigma_{ij} ds_{ij} + E_m dD_m \quad (1)$$

where σ_{ij} , s_{ij} are second rank mechanical stress and strain tensors respectively. E_m , D_m represents the vector of electric field and electric displacement respectively. The polarization P_m of the piezoelectric material is related to electric field E and electric displacement D by:

$$D_m = \epsilon_0 E_m + P_m \quad (2)$$

$$P_m = \epsilon_0 (\epsilon_r - I) E_m + e \mathcal{E} \quad (3)$$

$$P_m = \epsilon_0 \chi E_m + e \mathcal{E} \quad (4)$$

where χ represents the dielectric susceptibility of the piezoelectric material. Equations (3) and (4) show the relationship between the dielectric permittivity and temperature dependent susceptibility. The constitutive equation of the piezoelectric material can be derived using different types of thermodynamic potentials. Using the Gibbs electrical function as the thermodynamic potential, the stress charge form of the equation can be given by:

$$\sigma_{ij} = C_{ijkl} s_{kl} - e_{ijm} E_m \quad (5)$$

$$D_m = e_{mij} s_{ij} + \epsilon_{mk} E_k \quad (6)$$

The direct piezoelectric effect (or sensor mode effect) is given by equation (5) in which the electric displacement D_m is due to the applied mechanical stress. Inverse piezoelectric effect (actuator mode) is given by equation (6) which relates mechanical stress generated due to an electric field. The piezoelectric material modeled in this study, PZT 5A, exhibits a crystal structure with a symmetry of a hexagonal 6mm class. The piezoelectric material is considered transversely isotropic if the poling axis aligns with one of the material symmetry axes.

For a 2-D physics based model, 4 elastic coefficients, 3 piezoelectric coefficients and 2 dielectric coefficients of piezoelectric stiffness matrix are temperature dependent and given by:

$$C = \begin{bmatrix} c_{11} & c_{13} & 0 & 0 & e_{31} \\ c_{13} & c_{33} & 0 & 0 & e_{33} \\ 0 & 0 & c_{44} & e_{15} & 0 \\ 0 & 0 & e_{15} & -\varepsilon_{11} & 0 \\ e_{31} & e_{33} & 0 & 0 & -\varepsilon_{33} \end{bmatrix} \quad (7)$$

Further information regarding the temperature dependence of a piezoelectric material is given by Sabat et al. [24]. In the current mathematical model, the in-plane deformation problem is considered in the x-z plane as shown in Fig.1. Poling axis 3 of the PZT coincides with the y-axis of the model. Assumed electromechanical load for the in-plane problem is given by: a) $E_1 \neq 0, E_3 \neq 0, E_2 = 0$, also implies $D_1 \neq 0, D_3 \neq 0, D_2 = 0$ b) mechanical displacement $u_1 \neq 0, u_3 \neq 0, u_2 = 0$. Thus, the non-zero stress and strain components are given by $\sigma_{11}, \sigma_{33}, \sigma_{13}$ and s_{11}, s_{13}, s_{33} . The assumption (b) of non-zero mechanical displacement, strain, and stress also applies to linear elastic solids in the mathematical model.

3.2 Constitutive equation for the wave propagation in a linear elastic material

The equation of linear momentum balance in the time domain is given by

$$\rho \frac{\partial^2 u}{\partial t^2} = \nabla \cdot s + F_v \quad (8)$$

Where ρ is the assigned material density, u is the displacement, s is second order Piola-Kirchoff stress tensor, and F_v is the body force. The top boundary ($y=30$) for the Ω_{steel} shown in Fig. 1 is kept traction free ($\sigma_{31} = \sigma_{33} = \sigma_{11} = 0$). A low reflection boundary condition is applied to the Ω_{steel} at $x=0$ and $x=L$ boundaries to reduce reflection of the wave from side walls which also reduce the degree of freedom for which the model is solved, is given by:

$$\sigma \cdot n = -pC_p \left(\frac{\partial u}{\partial t} \cdot n \right) - pC_s \left(\frac{\partial u}{\partial t} \cdot t \right) \quad (9)$$

The vertices $x=0$ and $x=L$ on the bottom boundary ($y=0$) of the Ω_{steel} are modelled as fixed constraints ($u=0$) representing the fixed support used to ensure flatness of the structure during ultrasonic contact measurements. The boundary $y=L$ is assigned a normal characteristic acoustic impedance of air to simulate the acoustic impedance of the medium below the inspection sample.

3.3 Piezoelectric Material-Electrostatics

As previously stated, for the piezoelectric media, the electric field (piezoelectric media) is assumed to be irrotational. Thus, the electric field E is related to the scalar electric potential V by:

$$E = -\nabla V \quad (10)$$

$$n \cdot D = 0 \quad (11)$$

Terminal boundary is assigned to the top electrode of the piezoelectric material which is coupled to the external electrical circuit discussed in the next section. The bottom boundary of the Ω_{PZT} is grounded ($V=0$). Zero charge constraint is assigned in the domain Ω_{PZT} at boundaries without terminal or ground boundaries given by equation (11). Charge density ρ_v in the domain Ω_{PZT} is given by

$$\nabla \cdot D = \rho_v \quad (12)$$

3.4 External circuit for the instrumentation electrical impedance

In the experimental measurements, the piezoelectric transducer is connected to the pulsar-receiver circuit via BNC cables and lead wires. This introduces electrical impedance mismatch between the piezo and the instrumentation. This is modelled in a finite element model by introducing a resistor of impedance equal to that of pulsar-receiver. In the current study, the impedance value of resistor is set to an ideal 50 Ω . The electric circuit module in COMSOL evaluates global variables, voltage, and current as a function of time. In the current model, a Hamming windowed sinusoid signal of 160V is applied to the piezoelectric material. The current at the back electrode of the piezoelectric element $\partial^D \Omega_{pzt}$ is given by:

$$\int_{\partial^D \Omega_{pzt}} D \cdot n = Q_0, \frac{dQ_0}{dt} = I_{cir} \quad (13)$$

Hence the voltage on the electrode surface $\partial^D \Omega_{piezo}$ is given by:

$$V_{pz}(t) = V_{source}(t) - I_{cir}R \quad (14)$$

3.5 Discretization

A triangular element of maximum size 0.05mm was used for meshing the complete domain $\Omega = \Omega_{ss} \cup \Omega_{Transducer}$. The total number of elements is 256662 with an average growth rate of 1 and an average element quality equal to 0.99. The inside region of the SDH is not meshed. This simulates the defect as a geometric discontinuity. The maximum element size is determined by the minimum shear wave speed of the material assigned to the computational domain given by:

$$h_{max} = \frac{c}{f_0 N}, \quad t = \frac{CFL}{f_0 N} \quad (15)$$

where h_{max} is the maximum element size, c is the shear wave speed in the material, f_0 is the highest frequency in the desired spectrum, N is the number of element per wavelength, t is the time step, and CFL is set equal to 0.2.

3.6 Probability of detection formulation

The reflected signal displacement data from the physics based model corresponds to response \hat{a} . The true size (here, diameter) of the flaw a is related to response \hat{a} by

$$\hat{a} = \beta_0 + \beta_1 a \quad (16)$$

which is of the form

$$\hat{y} = \beta_0 + \beta_1 x \quad (17)$$

Equation (17) is also of the form $Ax=b$. Using the theory of least square solutions from linear algebra, the estimate for β_j is given by as:

$$\begin{bmatrix} \hat{\beta}_0 \\ \hat{\beta}_1 \end{bmatrix} = (A^T A)^{-1} A^T b \quad (18)$$

If system noise n is added to the equation (17), the modified equation (17) is then given as:

$$\hat{y}_1 = \beta_0 + \beta_1 x + n \quad (19)$$

where system noise n has a normal distribution $N(0, \tau^2)$. Using Bessel's correction, τ^2 is given by:

$$\tau^2 = \frac{1}{n-1} \sum (\hat{y}^2 - \hat{y}_1^2) \quad (20)$$

Using the Wald method, given in the standard handbook, MILHDBK-1823 A (Appendix G) [25]

$$\text{var}(\hat{y}) = \text{var}(\hat{\beta}_0) + x^2 * \text{var}(\hat{\beta}_1) + 2x * \text{COV}(\hat{\beta}_0, \hat{\beta}_1) \quad (21)$$

$$\text{var}(\hat{y}_1) = \text{var}(\hat{y}) + \tau^2 \quad (22)$$

The decision threshold y_{th} is set-up hypothetically by trial and error so that POD curves exhibit a typical nature observed in experimental PODs. The detection threshold is expressed as the amplitude of vertical displacement field from the model data. The upper and lower 95% confidence bounds are plotted using the Probit function. The POD curve is computed by the equation given as,

$$POD = \Phi \left(\frac{\hat{\beta}_0 + \hat{\beta}_1 x - y_{th}}{\sqrt{\text{var}(\hat{y}) + \tau^2}} \right) \quad (23)$$

Where Φ is the cumulative distribution function. It should be noted that \hat{y} is the displacement amplitude response from the SDHs computed using the physics based model described previously.

4 RESULTS AND INTERPRETATION

4.1 Model validation and Experimental verification

In this study, benchmark problem-SDHs ranging from 0.23mm to 3.9mm in diameter were considered. For the experimental verification SDHs are machined into a 1018 low carbon steel block except the 0.23mm diameter SDH. Pulse-echo contact measurements were performed with V306 Panametrics 2.25 MHz piezoelectric transducer with 12.7 mm nominal element diameter. The minimum distance between two adjacent SDHs is 22mm (greater than the beam width). As the defect size approaches the transducer beam width, the response is not a function of size of defect, but a function of reflection ratio and beam width [5] [15]. Hence, the largest flaw size was limited to 3.9mm to circumvent the effects of beam limitation.

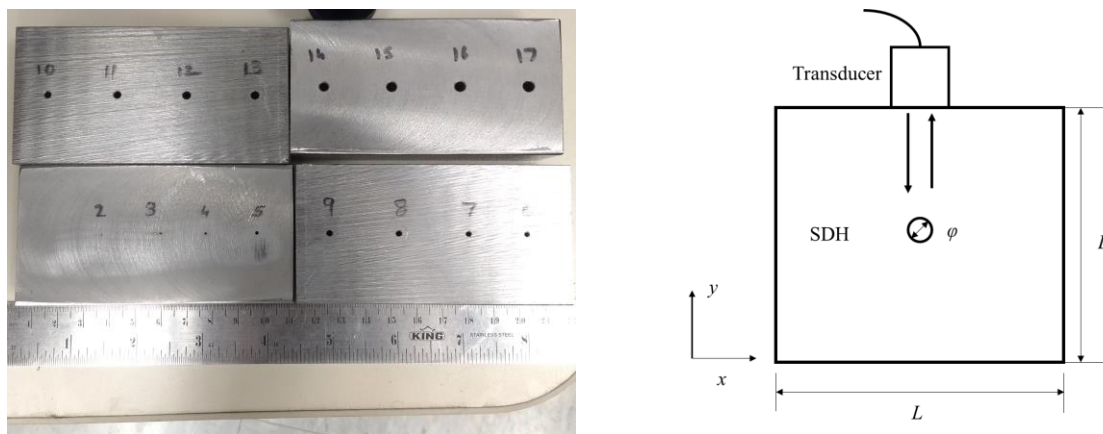


Figure 2. Side drilled holes with diameter varying from 0.46mm to 3.9 mm in a 1018 low carbon steel block

Contact measurement for each SDH is repeated 6 times for all 16 SDH to minimize the variability due to contact pressure. The Panametrics 5052 pulsar receiver is used with energy setting at 2, repetition rate at 4, 40 dB gain and damping set at 5. The experimental data is averaged 512 times and acquired using LeCroy HDO 4034 oscilloscope with sampling frequency 450MHz. Mean scattering amplitude response (\bar{x}) of each SDH is computed for validation with model based data. The experimental error for each SDH response

is given by $e = \sigma/\sqrt{N}$ where σ is the standard deviation and N is the number of measurements for each SDH. Mean value of experimental error (\bar{e}) is assigned to the experimental data points as $(\bar{x}) \pm (\bar{e})$, as shown in Fig.3(b).

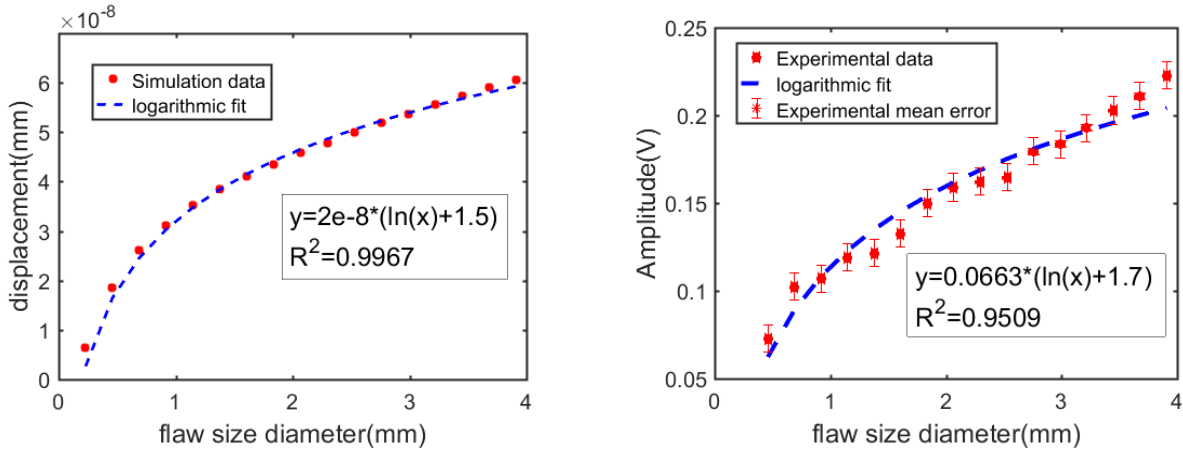


Figure 3. Scattering amplitude for a) Simulation data b) Experimental data

Fig.3(a) shows scattering amplitude from finite element model. Increase in the flaw size increases scattering amplitude which is fitted logarithmically in the form given by $y = m(\ln(x) + c)$ as shown in Fig. 3(a-b). However, the simulation data obtained is the vertical component of mechanical displacement field u from equation (8). The experimental data shown in Fig.3(b) is acquired in terms of amplitude voltage. Thus, to compare the scattering amplitude from experimental and simulation data, it is necessary to eliminate the effect of the pulsar-receiver settings on the scattering amplitude. Moreover, the scattering amplitude from the simulation is also dependent on the amplitude of the input mechanical displacement to the model. Hence, to eliminate these discrepancies in the measuring unit of scattering amplitudes, scaling and dimensional analysis of fitted data is performed. Hence, the corrected amplitudes y'_{sim} and y'_{exp} are given by

$$y'_{sim} = \frac{y_{sim}}{m_1} = \frac{y_{sim}}{2e-8} \approx \ln(x) + 1.5 \tag{24}$$

$$y'_{exp} = \frac{y_{exp}}{m_2} = \frac{y_{exp}}{0.0663} \approx \ln(x) + 1.7 \tag{25}$$

Fig.4 shows a good agreement between simulation and experimental data for the scattering amplitude of the SDHs. The transfer factors m_1 and m_2 from equation (24) and (25) are used to transform temperature effect from physics based model to the experimental POD which will be discussed in detail.

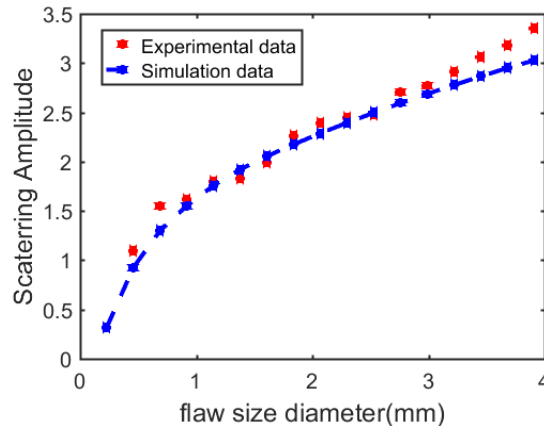


Figure 4. Scattering amplitude model validation with Experimental data using dimensional analysis

4.3 Model data for scattering amplitude variation due to temperature dependency of PZT-5A

In this model case, the transducer elements are modeled and temperature dependency is assigned to the piezoelectric material matrix, C , shown in equation (7). The material coefficients corresponding to a particular temperature are based upon the temperature dependent material coefficient in the literature [24].

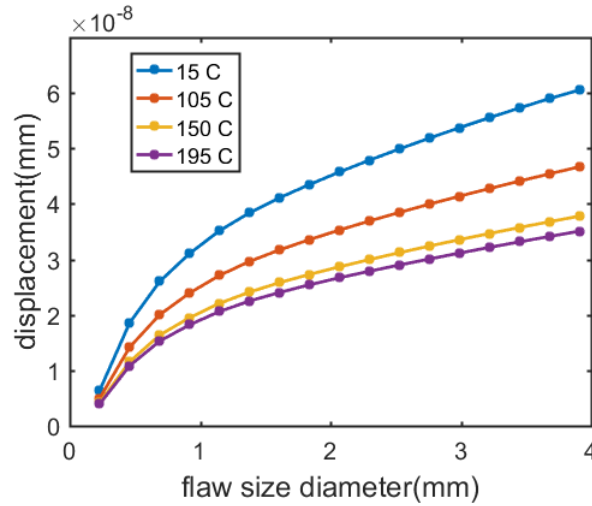


Figure 5. Displacement versus flow size (diameter) when using temperature dependent experimental data values for the piezoelectric material coefficients

The change in the flaw response as a function of temperature dependent response of the transducer is shown in Fig.5. It can be seen that the transducer sensitivity decreases as the temperature increases. The temperature dependence of the stiffness matrix of the piezoelectric material in the transducer reduces the scattering amplitude of the SDH governed by equation (7) and (8). This reduces the displacement response received by the sensor as demonstrated by the Fig. 5. The logarithmic fitting of the simulated data in the form of equation (16) is shown in Table I.

Table I: Logarithmic fitting of the simulated data

Temperature	Equation	β_1	β_0
15 C	$\hat{a} = 1e-8(2 * \ln(a) + 3)$	2e-8	3e-8
105 C	$\hat{a} = 1e-8(1 * \ln(a) + 3)$	1e-8	3e-8
150 C	$\hat{a} = 1e-8(1 * \ln(a) + 2)$	1e-8	2e-8
195 C	$\hat{a} = 1e-8(1 * \ln(a) + 2)$	1e-8	2e-8

As the temperature increases from 15C to 105 C, β_1 reduces from 50% and β_0 remains unchanged. Increasing temperature of the piezoelectric material from 105 C to 150 C reduces the value of β_0 by 66% while the value of β_1 remains unchanged. It should be noted that from 150 C to 195 C there is no change in the equation used for logarithmically fitting the data.

4.3 Probability of detection (POD) curve with temperature dependence of the transducer

Using equations (16) through (23), POD values are calculated and the resulting data is plotted from the physics based model data for different temperatures. The detection threshold is expressed as the amplitude of vertical component of the mechanical displacement field u from the model data.

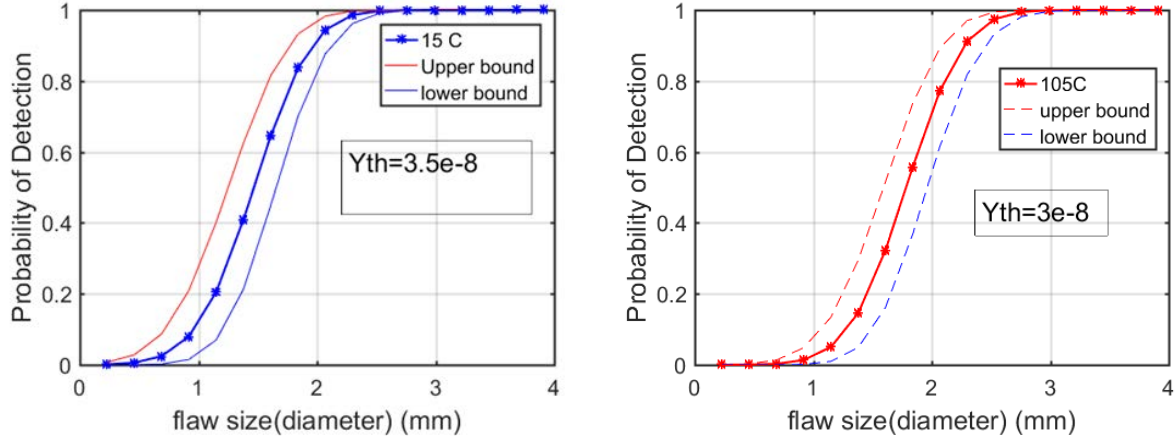


Figure 6. Probability of detection: a) 15 C b) 105 C for the predefined detection threshold Y_{th}

The probability value is found to be highly dependent on the decision threshold. In the current work, the detection threshold is set hypothetically to be able to represent a typical POD curve as shown in Fig. 6 and Fig.7. Fig 6 (a) through Fig. 7(b) show POD values for 15C, 105C,150C, and 195C. It should be noted that as the temperature is increased, the detection threshold needed to be lowered.

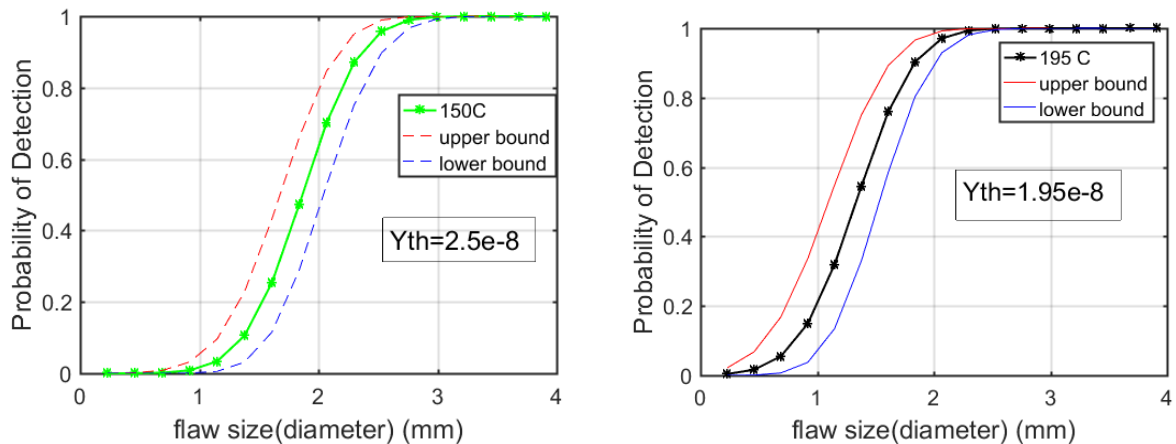


Figure 7. Probability of detection at: a) 150 C b) 195 C for the predefined detection threshold Y_{th}

However, the detection threshold is generally a system limitation which should be unmodified for all the temperature. Hence, Y_{th} is selected as $3.5e-8$ mm which corresponds to the threshold at 15 C. Fig. 8 shows POD values for temperature increasing from 15 to 195 C. For the given decision threshold, the flaw size with $POD=1$ at 15C reduces significantly at 195C as shown in Fig.8. Hence, the current study can help determine the flaw sizes which see a reduction in probability due to the temperature dependent response of the piezoelectric transducer. It can be seen from Fig. 8 that, increase in the temperature of the transducer introduces a considerable source of variability in the POD for a given flaw size. Here, the POD reduces significantly for SDHs with a diameter between wavelength λ (1.4mm) and $7\lambda/6$ (3mm) in SS 316

at 2.25 MHz . For the specific example considered with a 3mm diameter SDH and at 2.25 MHz ($\sim 7\lambda/6$) and using PZT -5A properties, the POD exhibits a 90% reduction between response at 15 C and 195 C.

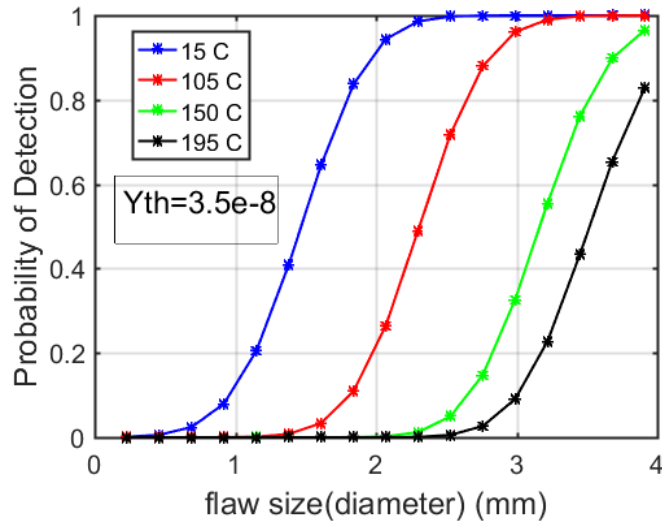


Figure 8. Effect of temperature dependence of piezoelectric transducer, with PZT -5A on the POD curve

Table II quantifies the effect of temperature dependency for PZT-5A piezoelectric material properties at 2.25 MHz on the POD Values. For artificial defects such as SDHs of size 2λ , a 97% reduction in the POD value between 15 C and 195 C can be seen due to the temperature effect on the piezoelectric material.

Table II. Model based data for POD as a function of transducer temperature and flaw size

Flaw size(mm)	POD ($Y_{th}=3.5e-8$)			
	15 C	105 C	150 C	195 C
0.23 ($\lambda/6$)	0.001	0	0	0
0.46 ($\lambda/3$)	0.005	0	0	0
0.69($\lambda/2$)	0.024	0	0	0
0.92	0.08	0.0001	0	0
1.15	0.21	0.001	0	0
1.38 (λ)	0.41	0.008	0	0
1.61	0.64	0.033	0	0
1.84	0.84	0.11	0	0
2.07	0.94	0.26	0.002	0
2.3	0.99	0.49	0.012	0
2.53	1	0.72	0.05	0.006
2.76 (2λ)	1	0.88	0.15	0.03
2.99	1	0.96	0.33	0.091
3.22	1	0.99	0.55	0.23
3.45(2.5λ)	1	1	0.76	0.43
3.68	1	1	0.9	0.65
3.91 (2.8λ)	1	1	0.96	0.83

4.4 Temperature correction Factor K

In sections 4.1 through 4.3, the material coefficients for PZT-5A are altered based on the temperature dependent experimental data [24] at corresponding temperatures. The effect of the temperature dependent coefficients on the scattering amplitude of SDHs is quantified by the finite element model shown in Fig.5 and Fig.8. In this section, using the simulated data for temperature dependent scattering amplitudes, a correction factor K for the temperature effect of PZT-5A is proposed which is calculated by the dividing the scattering amplitudes at 15C by the scattering amplitude at corresponding temperature. The numerical uncertainty in the correction factor is $K \pm 0.02$ with maximum deviation at SDH of 0.23mm diameter.

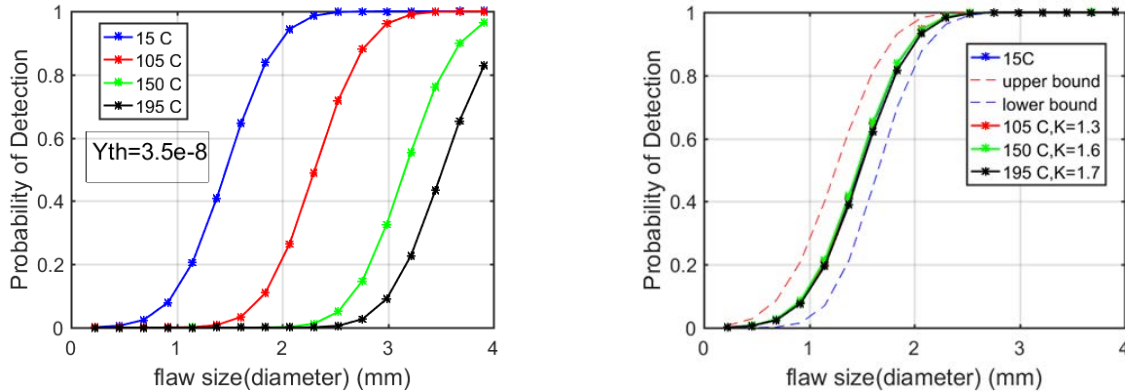


Figure 9. Model based POD a) Without correction factor b) With PZT-5A temperature correction factor K . (dashed line (red, blue) indicate 95% confidence bounds for POD curve at 15 C

As shown in Fig. 9(b), the value of K at corresponding temperatures is the magnitude by which scattering amplitude needs to be compensated to match POD at 15C. Fig.10 shows the POD for experimental data at room temperature. In order to apply temperature correction factor from physics based model, to the actual experimental data, the detection threshold voltage for the experimental POD is formulated as

$$V_{th} = \frac{Y_{th}}{m_1} * m_2 = 0.1160 \approx 0.12V \quad (26)$$

where $Y_{th} = 3.5e-8$ (mm) is detection threshold for the model data and the transfer factors m_1 , m_2 were obtained from equation (24) and (25). Now, using this temperature specific factor K , reduction in the scattering amplitudes of room temperature experimental data is calculated for 105C, 150C, and 195C. In this way, Fig. 10 shows the estimation of high temperature (HT) POD using room temperature experimental data, correction factor K and transfer factors m_1 , and m_2 .

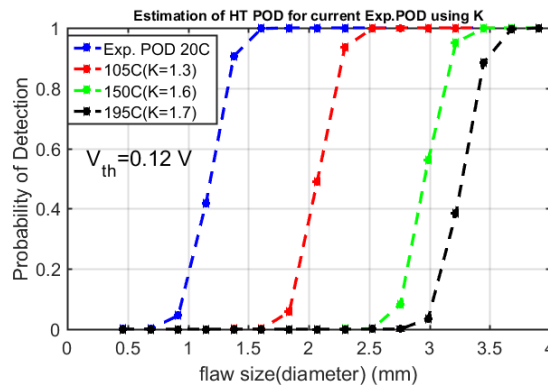


Figure 10. Estimation of High temperature (HT) POD using room temperature experimental POD (dashed blue line) with temperature correction factor for PZT-5A, obtained from the physics based model

As shown in Fig. 10, 97% reduction in the POD of room temperature experimental data is estimated at 195C for SDHs of diameter from 1.5mm to 2.8 mm using this model based POD approach.

5 CONCLUSION

Current work demonstrated a finite element pulse echo model for scattering due to a cylindrical side drilled hole in a steel specimen. The simulated amplitude response from SDHs is in good agreement with the experimental data after correcting for experimental and numerical uncertainties. In both experimental and simulated data, near unity value of coefficient of determination (R^2) indicated that the scattering amplitude due to SDH can be well represented by a logarithmic fitting and as a function of a hole diameter. Changes in the material coefficients of the piezoelectric material as a function of temperature, reduced the scattering amplitude for the given size of SDH. This changed the slope and intercept of the logarithmically fitted data. The detection threshold for the simulation based POD needed to be lowered as the temperature increased from 15C to 195C. For a constant threshold value, significant reduction in POD was predicted, particularly in the SDHs with diameter from 1.6 mm to 3mm. For SDH of 2.8mm diameter, a 97% reduction in POD value was estimated due to the temperature effect on material coefficients of PZT-5A from 15C to 195C.

A temperature correction factor is proposed using scattering amplitudes estimated for 15C, 105C, 150C, and 195C from the physics based model. This correction factor represented the change in the material coefficients of PZT-5A due to temperature dependent intrinsic and extrinsic contributions within the piezoelectric ceramic at a high temperature. Using the transfer factors obtained from experimental and simulated data, a detection threshold is formulated to calculate POD for experimental data at room temperature. Finally, using this experimental data, temperature specific correction factor K and the transfer factors m_1 , and m_2 , a model based approach has been demonstrated to estimate POD at high temperature using low temperature ultrasonic pulse-echo measurements.

ACKNOWLEDGEMENT

This work is funded by the U.S. Department of Energy's office of Nuclear Energy under Nuclear Energy University programs (NEUP) and performed at the Centre for NDE at Iowa State University. The authors would like to acknowledge the assistance of Dr. Sabat (Department of Physics, Royal Military College of Canada, Kingston, Ontario K7K 7B4, Canada) [24] who provided the experimental material property data for PZT-5A (EC-65). The authors would also like to acknowledge support of Bill Halterman and Bruce Erickson (Chemistry Machine Shop, Iowa State University) for machining of side drilled holes in the steel specimens.

REFERENCES

1. OECD "Technology roadmap update for generation IV nuclear energy systems," OECD Nuclear Energy Agency for the Generation IV International Forum (2014). <https://www.gen-4.org/gif/upload/docs/application/pdf/2014-03/gif-tru2014.pdf>
2. CEA "4th-generation sodium-cooled fast reactors The ASTRID Technological Demonstrator," Direction de l'énergie nucléaire (nuclear energy division), Centre de Saclay, CEA (2012)
3. Griffin, J. W., Peters, T. J., Posakony, G. J., Chien, H. T., Bond, L. J., Denslow, K. M., Sheen, S. H. and Raptis, P. "Under-Sodium viewing: a review of ultrasonic imaging technology for liquid metal fast reactors," PNNL-18292, Pacific Northwest National Laboratory, Richland, WA (2009).
4. Meeker, W. Q. "RB Thompson's contributions to model assisted probability of detection". In *Proc. Review of Progress in Quantitative Nondestructive Evaluation*: Vol. 31, AIP Conference Proceedings # 1430, No. 1, pp. 83-94. AIP Publishing (2012)
5. Sarkar, P., Meeker, W. Q., Thompson, R. B., Gray, T. A., and Junker, W. "Probability of detection modeling for ultrasonic testing" In *Proc. Review of Progress in Quantitative Nondestructive Evaluation*, Vol.17, Plenum press, New York, pp. 2045-2052, Springer US (1998).
6. Thompson, R. B. "A Unified Approach to The Model-Assisted Determination of Probability of Detection". In D. O. Thompson, & D. E. Chimenti (Eds.), *AIP Conference Proceedings*, Vol. 975, No. 1, pp. 1685-1692 (2008)

7. Thompson, R. Bruce; Brasche, Lisa H.; Forsyth, D.; Lindgren, E.; Swindell, P.; and Winfree, W., "Recent Advances in Model-Assisted Probability of Detection" *Proc. 4th European-American Workshop on Reliability of NDE* (2009)
8. Cobb, A. C., Fisher, J., and Michaels, J. E. "Model-assisted probability of detection for ultrasonic structural health monitoring". In *Proc. 4th European-American Workshop on Reliability of NDE* (2009)
9. Smith, K., Thompson, B., Meeker, B., Gray, T., and Brasche, L. "Model-Assisted Probability of Detection Validation for Immersion Ultrasonic Application". In D. O. Thompson, & D. E. Chimenti (Eds.), *AIP Conference Proceedings*, Vol. 894, No. 1, pp. 1816-1822 (2007).
10. Smith, K. D. "POD Transfer Function Approach". In *MAPOD Working Group Meeting*, Vol. 4 (2005).
11. Aldrin, J. C., Medina, E. A., Lindgren, E. A., Buynak, C. F., and Knopp, J. S. "Protocol for reliability assessment of structural health monitoring systems incorporating model-assisted probability of detection (MAPOD) approach" Air Force Research Lab Wright-Patterson AFB Materials and Manufacturing Directorate (2011).
12. Jensen, F., Mahaut, S., Calmon, P., and Poidevin, C. "Simulation based POD evaluation of NDI techniques". In *Proc 10th European Conference on Non-destructive Testing* (2010).
13. Wirdelius, H., and Persson, G. "Simulation based validation of the detection capacity of an ultrasonic inspection procedure" *International Journal of Fatigue*, **41**, pp 23-29 (2012).
14. Pavlovi, M., Takahashi, K., and Müller, C. "Probability of detection as a function of multiple influencing parameters" *Insight-Non-Destructive Testing and Condition Monitoring*, **54**(11), pp 606-611 (2012).
15. Li, M., Meeker, W. Q., and Thompson, R. B. "Physical model-assisted probability of detection of flaws in titanium forgings using ultrasonic nondestructive evaluation" *Technometrics*, **56**(1), pp78-91 (2014).
16. Subair, S. M., Balasubramaniam, K., Rajagopal, P., Kumar, A., Rao, B. P., and Jayakumar, T., "Finite element simulations to predict probability of detection (PoD) curves for ultrasonic inspection of nuclear components" *Procedia Engineering*, **86**, 461-468 (2014)
17. Roy, S., Lonkar, K., Janapati, V., and Chang, F. K., "A novel physics-based temperature compensation model for structural health monitoring using ultrasonic guided waves" *Structural Health Monitoring*, **13**(3), 321-342 (2014).
18. Wang, Y., Gao, L., Yuan, S., Qiu, L., and Qing, X. "An adaptive filter-based temperature compensation technique for structural health monitoring" *Journal of Intelligent Material Systems and Structures*, **25**(17), pp2187-2198 (2014)
19. Salmanpour, M. S., Khodaei, Z. S., and Aliabadi, M. H. "Guided wave temperature correction methods in structural health monitoring" *Journal of Intelligent Material Systems and Structures*, **28**(5), pp 604-618 (2017).
20. Gianneo, A., Carboni, M., Müller, C., and Ronneteg, U. "UPAUT inspection of copper canister: Structural attenuation and POD formulation" In *Review of Progress in QNDE*, Vol. 35, D. E. Chimenti, and L. J. Bond (Eds.), *AIP Conference Proceedings* # 1706, paper 200005, AIP Publishing (2016).
21. Gianneo, A., Carboni, M., and Giglio, M. "Feasibility study of a multi-parameter probability of detection formulation for a Lamb waves-based structural health monitoring approach to light alloy aeronautical plates" *Structural Health Monitoring*, **16**(2), pp. 225-249 (2017).
22. Yusa, N., Chen, W., and Hashizume, H. "Demonstration of probability of detection taking consideration of both the length and the depth of a flaw explicitly" *NDT&E International*, **81**, pp 1-8 (2016).
23. Janapati, V., Kopsaftopoulos, F., Li, F., Lee, S. J., and Chang, F. K., "Damage detection sensitivity characterization of acousto-ultrasound-based structural health monitoring techniques" *Structural Health Monitoring*, **15**(2), pp143-161 (2016).
24. Sabat, R. G., Mukherjee, B. K., Ren, W., and Yang, G. "Temperature dependence of the complete material coefficients matrix of soft and hard doped piezoelectric lead zirconate titanate ceramics" *Journal of Applied Physics*, **101**(6), 06411 (2007)
25. U.S. Department of Defense, MIL-HDBK-1823A Nondestructive Evaluation System Reliability Assessment, Appendix G (2010).